



# A high-capacity aqueous zinc-ion battery fiber with air-recharging capability†

Cite this: *J. Mater. Chem. A*, 2021, 9, 6811

Received 28th January 2021  
Accepted 28th February 2021

DOI: 10.1039/d1ta00803j

rsc.li/materials-a

Meng Liao, Jiawei Wang, Lei Ye, Hao Sun, Pengzhou Li, Chuang Wang, Chengqiang Tang, Xiangran Cheng, Bingjie Wang\* and Huisheng Peng \*

Flexible fiber batteries with self-powering functionality will offer new opportunities for next-generation wearable electronic devices. Here, we present a high-capacity aqueous Zn-ion battery fiber that can directly harvest energy from ambient air to recharge without using additional power supply. The air-recharging capability stems from the freestanding cathode fiber consisting of nano-structured  $V_6O_{13}$ /aligned carbon nanotubes, which can induce a spontaneous redox reaction with ambient air at its discharged state for capacity recovery. This air-recharging process is reversible and compatible with the routine galvanostatic charge–discharge of aqueous Zn-ion batteries. The resultant battery fiber shows a high specific capacity ( $371 \text{ mA h g}^{-1}$  at  $200 \text{ mA g}^{-1}$ ), stable cyclability (91% capacity retention after 5000 cycles at  $5 \text{ A g}^{-1}$ ), and can be efficiently recharged to  $\sim 60\%$  upon exposure to air. Finally, we demonstrate a self-charging battery fiber to effectively power a strain sensor in an integrated, wearable fingertip.

## Introduction

The widespread use of mobile and wearable electronic devices has driven the demand for flexible power solutions that are light and compact.<sup>1,2</sup> Fiber batteries are promising because they are durable, light-weight and can be woven into textiles.<sup>3</sup> However, it is challenging for fiber batteries to escape from the limited duration to meet the ever-increasing power demand of wearable devices.<sup>4–6</sup> Moreover, the recharge and reuse of fiber batteries are restricted when the electricity power is unavailable, *e.g.*, in outdoor usage scenarios, which are frequent occurrences for wearable electronics.<sup>7</sup> To tackle above-mentioned limitations, numerous energy harvesting components including solar cells, triboelectric generators and biofuel cells have been integrated with fiber batteries into self-powered systems.<sup>8–12</sup> However, they

highly rely on specific energy resources, *e.g.*, constant sunlight, frequent motions and large amount of sweat, which are sometimes unavailable to recharge the fiber batteries. Besides, external connections and accessories are required in such systems, reducing the advantageous flexibility and applicability of fiber batteries.

Other than the integration at the device level, designing self-chargeable electrode materials represents a promising option. Recent investigation have shown that several active redox materials, such as Prussian blue, tungsten oxides, polypyrrole and vanadium-based compounds, can be utilized for self-powered electrodes in planar electrochromic and energy storage devices due to their spontaneous oxidation reactions in ambient conditions.<sup>13–18</sup> Thus, by employing such electrode materials, self-charging fiber batteries with simplified device configuration, being highly independent of usage scenarios, can be expected. However, the reported self-chargeable materials are assembled in rigid, open-structure devices, and show either limited capacity ( $<100 \text{ mA h g}^{-1}$ ), poor reversibility, or inadequate efficiency. To date, there are no self-charging fiber batteries due to the bottlenecks of materials design and configuration-based solution, *e.g.*, it is critical but difficult to synthesize electrode materials that possess good properties for both energy storage and self-charging; it is of course more difficult to achieve self-charging fiber batteries in flexible, compact configuration to afford reliable performances against various deformations and ambient erosions.

Here, we report a high-capacity, aqueous Zn-ion battery fiber that can be self-recharged in ambient air (Fig. 1a). As a key component, the self-chargeable fiber electrode was prepared by synthesizing nano-textile-like  $V_6O_{13}$  onto the aligned carbon nanotube (CNT) fiber *via* a facile solution-redox method. Nano-structured  $V_6O_{13}$  is redox-active in a wide range of oxidation states, and can afford abundant active sites for  $\text{Zn}^{2+}$ -storage to achieve high capacity.<sup>19</sup> The freestanding  $V_6O_{13}$ /CNT hybrid fiber (VCF) is directly assembled as a cathode with a Zn anode fiber to produce the self-charging VCF/Zn battery fiber with high flexibility. We discover that the discharged VCF can be

State Key Laboratory of Molecular Engineering of Polymers, Department of Macromolecular Science, Laboratory of Advanced Materials, Fudan University, Shanghai 200438, China. E-mail: wangbingjie@fudan.edu.cn; penghs@fudan.edu.cn  
† Electronic supplementary information (ESI) available. See DOI: 10.1039/d1ta00803j

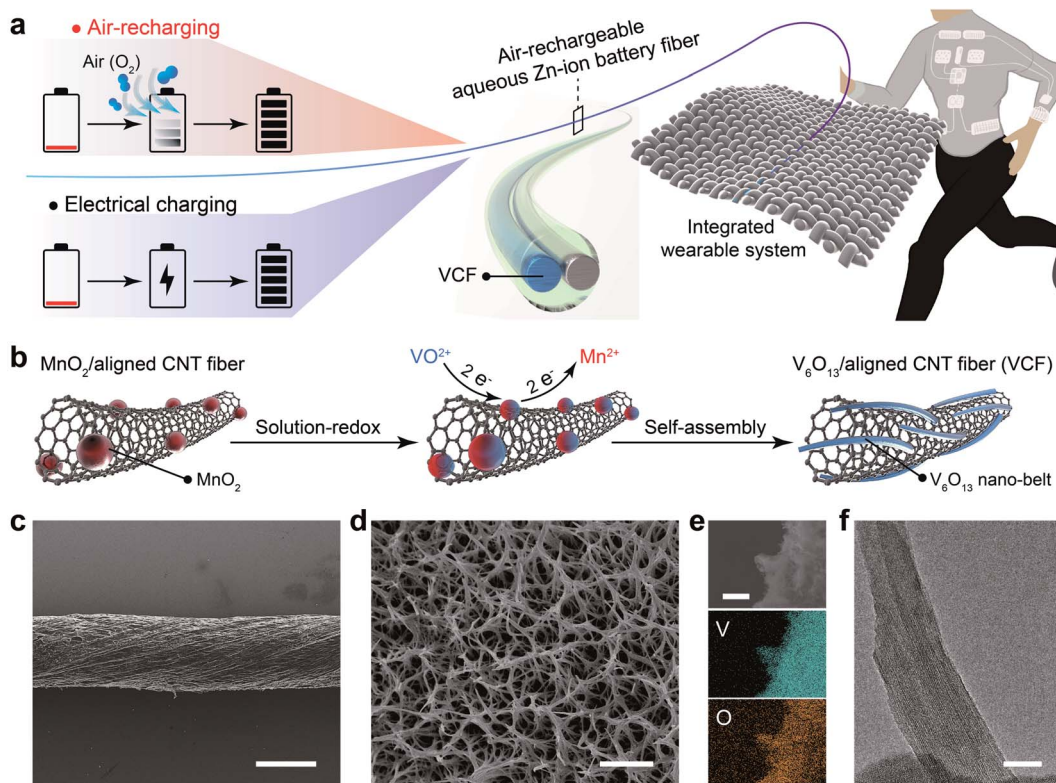


Fig. 1 (a) Schematic of the aqueous Zn-ion battery fiber with air-recharging capability integrated into multifunctional wearable systems. (b) Schematic of the synthesis and formation of the freestanding V<sub>6</sub>O<sub>13</sub>/aligned CNT cathode fiber (VCF) in the air-rechargeable aqueous Zn-ion battery fiber. (c) and (d) Scanning electron microscopy images of VCF at low and high magnifications, respectively. (e) Energy dispersive spectrometer mappings of VCF. (f) A bright-field transmission electron microscopy image of V<sub>6</sub>O<sub>13</sub> nanobelts anchored on VCF. Scale bars, 100 μm in (c), 1 μm in (d), 10 μm in (e) and 20 nm in (f).

converted to its charged state with capacity recovery *via* a spontaneous oxidation reaction with air (O<sub>2</sub>). We refer to such a reaction as an air-recharging process, which is available in numerous environments since air is pervasive in our living space. An exceptional deintercalation mechanism, other than the conversion in previous self-chargeable electrodes, is demonstrated in the air-recharging process of VCFs. Constructing this air-rechargeable battery fiber in the paradigm of aqueous Zn-ion batteries (ZIBs)<sup>19–24</sup> further offers several advantages including high specific capacity, safety and glove-free fabrication. In addition, a flexible, tubular low-density polyethylene encapsulation is designed to inhibit the fiber battery from electrolyte volatilization and moisture erosion in ambient air. The resultant air-recharging VCF/Zn battery fiber delivers a high specific capacity (371 mA h g<sup>-1</sup> at 200 mA g<sup>-1</sup>), stable cyclability (91% capacity retention after 5000 cycles at 5 A g<sup>-1</sup>), and can be efficiently recharged to ~60% upon exposure to air without additional power supply.

## Results and discussion

The synthesis of VCF designed for air-rechargeable ZIB fiber is schematically illustrated in Fig. 1b. Aligned CNT fibers obtained from a continuous floating catalyst chemical vapor deposition method<sup>25</sup> (details in Note S1†) were twisted in a multi-strand

manner and used as the fiber current collectors (Fig. S1 and S2†). V<sub>6</sub>O<sub>13</sub> was then grown onto the aligned CNT fibers *via* a facile solution-redox reaction at room temperature (Fig. S3–S5†). Our synthetic approach circumvented the prolonged heat treatment required for the routine hydrothermal synthesis of vanadium oxides as well as a multi-step coating method to further obtain the vanadium oxide-based electrode for ZIBs.<sup>26</sup> The freestanding, binder-free VCF with flexibility (Fig. S6†) may alleviate the exfoliation and cracking of active materials upon deformations and could be prepared in a scalable manner for the direct fiber battery assembly. Scanning electron microscopy (SEM) and energy-dispersive X-ray spectroscopy (EDS) analyses showed that the interconnected, porous network of as-synthesized V<sub>6</sub>O<sub>13</sub> nanobelts were uniformly anchored on the CNT fibers without discernible impurities (Fig. 1c–e and S7, S8†). The hierarchical CNT fibers increased the accessible surface area of VCFs (171.3 m<sup>2</sup> g<sup>-1</sup>) to the electrolyte (Fig. S9†), enhancing not only the transport of electrons and Zn<sup>2+</sup> ions for improved cathode utilization (Fig. S10†) but also the O<sub>2</sub> absorption to activate the air-recharging reaction. Transmission electron microscopy (TEM) images further evidenced the anisotropic V<sub>6</sub>O<sub>13</sub> structure with layer-spacing parallel to the length direction of nanobelts (Fig. 1f and S11, S12†).

Since the air-recharging process is based on the discharged cathode material, VCF was first paired with the Zn anode fiber

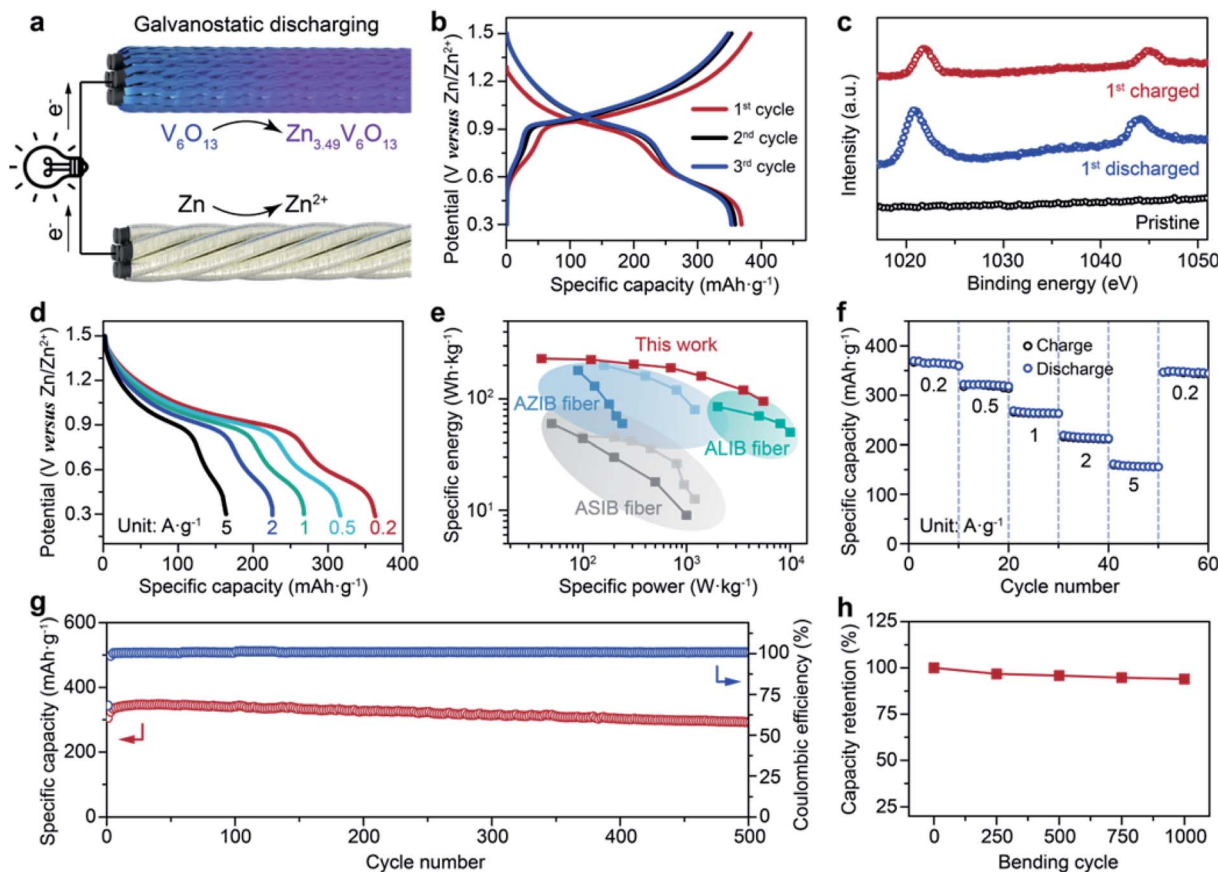


**Fig. 2** (a) Schematic to the VCF/Zn battery fiber during galvanostatic discharge. (b) Galvanostatic charge–discharge curves at  $200 \text{ mA g}^{-1}$  for the first three cycles of the VCF/Zn battery fiber. (c) X-ray photoelectron spectroscopy of Zn 2p at pristine, fully discharged, and charged states. (d) Galvanostatic discharge profiles of VCF at increasing current densities from 200 to  $5000 \text{ mA g}^{-1}$ . (e) Comparison of the Ragone plot of the VCF/Zn battery fiber with other state-of-art aqueous battery fibers, e.g., aqueous Li-ion battery (ALIB), aqueous Na-ion battery (ASIB) and aqueous Zn-ion battery (AZIB) fibers.<sup>31–35</sup> In this figure, the energy values were calculated on the basis of the mass loading of cathode materials by integrating the voltage profile during discharge. (f) Rate capability of VCF upon increasing current densities. (g) Cycling performance of VCF at  $500 \text{ mA g}^{-1}$ . (h) Dependence of the capacity retention on the bending cycle of the VCF/Zn battery fiber.

to fabricate the VCF/Zn battery fiber (Fig. 2a and S13<sup>†</sup>) for the electrochemical evaluation. A high initial discharge capacity of  $371 \text{ mA h g}^{-1}$  was achieved at  $200 \text{ mA g}^{-1}$  (based on the mass loading of  $\text{V}_6\text{O}_{13}$ ) with an average plateau of  $\sim 0.78 \text{ V}$  (Fig. 2b and S14<sup>†</sup>). The normalized capacity of the VCF/Zn battery fiber was  $0.74 \text{ mA h cm}^{-1}$  at  $0.4 \text{ mA cm}^{-1}$  and could be further enhanced by increasing the mass loading of  $\text{V}_6\text{O}_{13}$  in VCFs. The reversible  $\text{Zn}^{2+}$  storage/release was evidenced by the appearance of pronounced Zn 2p peaks at 1021.3 eV ( $2p_{3/2}$ ) and 1044.1 eV ( $2p_{1/2}$ ) in the fully discharged VCF, which were not detected in the pristine VCF (Fig. 2c).<sup>27,28</sup> These Zn 2p peaks then became weak upon charging, suggesting the extraction of  $\text{Zn}^{2+}$  ions from VCF. The *in situ* X-ray diffraction (XRD) measurement further showed an enlarged *d*-spacing of  $\text{V}_6\text{O}_{13}$  during the discharge (Fig. S15<sup>†</sup>), which indicated the large accommodation of  $\text{Zn}^{2+}$  in the layer-structured  $\text{V}_6\text{O}_{13}$  and so as the high discharge capacity.<sup>29,30</sup> An insertion of up to  $\sim 3.49$  Zn per unit formula of  $\text{V}_6\text{O}_{13}$  was determined in a fully discharged VCF, *i.e.*,  $\text{Zn}_{3.49}\text{V}_6\text{O}_{13}$  (Fig. S16<sup>†</sup>). Moreover, VCF showed high rate capability (Fig. 2d) with a specific energy up to  $\sim 230 \text{ W h kg}^{-1}$ , outperforming the previously reported aqueous battery fibers

(Fig. 2e).<sup>31–35</sup> The capacity could immediately recover with the reversal of the applied current density from 5 to  $0.2 \text{ A g}^{-1}$  for over 60 cycles (Fig. 2f). Such facilitated kinetics in VCFs was attributed to a high surface-controlled capacity contribution<sup>36–38</sup> of up to 93.4% from the cyclic voltammetry (CV) studies (Fig. S17<sup>†</sup>). With the above-mentioned merits, the VCF/Zn fiber could maintain a capacity of  $\sim 310 \text{ mA h g}^{-1}$  at  $0.5 \text{ A g}^{-1}$  over 500 cycles (Fig. 2g), or a capacity of  $\sim 151 \text{ mA h g}^{-1}$  at  $5 \text{ A g}^{-1}$  over 5000 cycles (Fig. S18<sup>†</sup>). Moreover, the flexible fiber-shaped configuration rendered the VCF/Zn battery with high durability, enabling a well-maintained output under increasing bending angles from 0 to  $180^\circ$  (Fig. S19<sup>†</sup>). Even after 1000 cycles of bending (Fig. 4h) and twisting (Fig. S20<sup>†</sup>), the battery fibers retained over 90% of the original capacity.

The air-recharging capability was determined to stem from the spontaneous oxidation of the discharged VCF upon its exposure to  $\text{O}_2$  (Fig. 3a). In the routine galvanostatic charging process driven by electrical grid (schematic in Fig. S21<sup>†</sup>), electrons are released from the discharged (reduced) cathode, leading to oxidized vanadium in the cathode along with extracted  $\text{Zn}^{2+}$  from the layered structure.<sup>21,39</sup> Alternatively, we

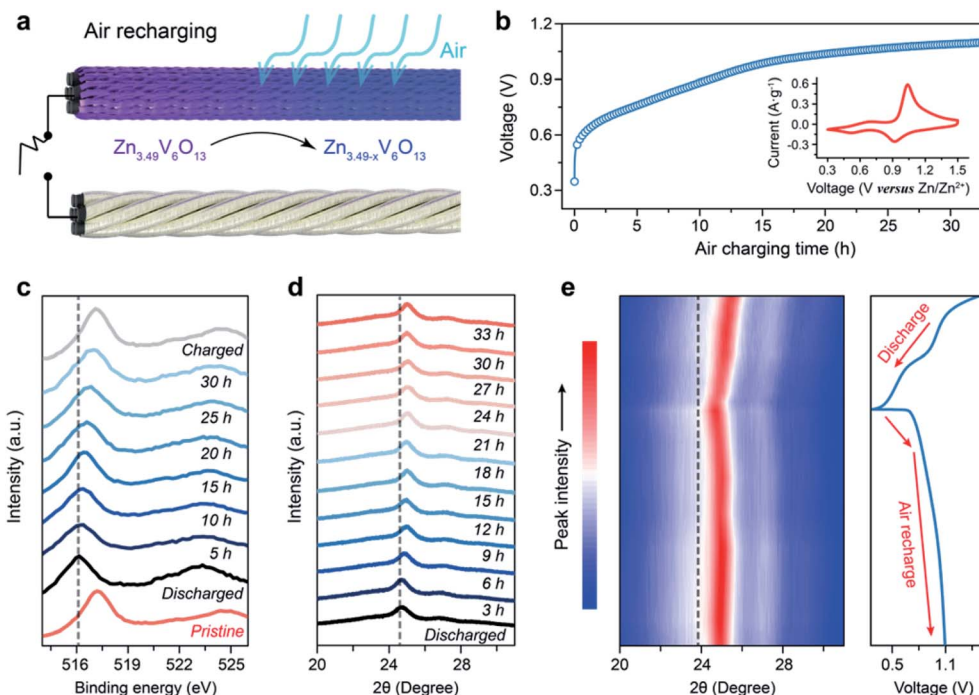


**Fig. 3** (a) Schematic to the VCF/Zn battery fiber during an air-recharging process. (b) Voltage–time curve of the VCF/Zn battery fiber upon the air-recharging process (inset, typical cyclic voltammogram at  $0.2 \text{ mV s}^{-1}$  of the VCF/Zn battery fiber). (c) V 2p X-ray photoelectron spectroscopy of the fully discharged VCF at different states in the air-recharging process. (d) *In situ* X-ray diffraction patterns of the discharged VCF at various air-recharging states. (e) *In situ* X-ray diffraction patterns of VCF during the galvanostatic discharge ( $100 \text{ mA g}^{-1}$ ) and the sequent air-recharging process.

discovered that the discharged VCF (e.g.,  $\text{Zn}_{3.49}\text{V}_6\text{O}_{13}$ ) with low-valence-state vanadium could be spontaneously oxidized by  $\text{O}_2$  in air to its charged state ( $\text{Zn}_{3.49-x}\text{V}_6\text{O}_{13}$ ) with the release of  $\text{Zn}^{2+}$  for the charge balance (Fig. 3a). Along this line, the fully discharged product could recover to its charged state without any external power supply in the VCF/Zn battery fibers. This spontaneous oxidation reaction could be theoretically explained by the redox potential difference between the discharged VCF (low to  $-0.24 \text{ V}$  versus standard hydrogen electrode) and the oxygen dissolved in the aqueous mildly acidic electrolyte ( $\sim 1.23 \text{ V}$  versus standard hydrogen electrode) obtained from the cyclic voltammogram (Fig. 3b).<sup>40</sup> Considering the acidic condition in the  $3 \text{ M Zn}(\text{CF}_3\text{SO}_3)_2$  electrolyte, the existing  $\text{H}^+$  ions would induce the reduction of dissolved  $\text{O}_2$  to  $\text{H}_2\text{O}$ . Moreover, the discharged VCF ( $\text{Zn}_{3.49}\text{V}_6\text{O}_{13}$ ) would be oxidized by  $\text{O}_2$  with the release of  $\text{Zn}^{2+}$  ions (details in Note S3<sup>†</sup>). Experimentally, this air-recharging process was first discovered from an increasing open-circuit voltage (OCV) attributed to the gradually deeper oxidation (Fig. 3b) in a fully discharged VCF/Zn battery with exposure to  $\text{O}_2$ . Note that the above air-recharging reaction would not take place in the absence of  $\text{O}_2$ , i.e., the VCF/Zn battery fiber delivered limited OCV ( $<0.6 \text{ V}$ ) and capacity recovery ( $<5 \text{ mA h g}^{-1}$ ) after exposure to an  $\text{O}_2$ -eliminated condition for 20 h (Fig. S22<sup>†</sup>).

X-ray photoelectron spectroscopy (XPS) was further used to elucidate the air-recharging reaction of the fully discharged VCFs in  $3 \text{ M Zn}(\text{CF}_3\text{SO}_3)_2$  aqueous electrolyte with dissolved  $\text{O}_2$  (Fig. 3c). With the increasing air-recharging time from 0 (fully

discharged VCF) to 30 h, V 2p peaks were found to be gradually shifted to higher binding energy, suggesting the oxidation of V elements in the discharged VCFs. This oxidation was accompanied by the extraction of  $\text{Zn}^{2+}$  ions from the layered structure in the discharged VCFs, as revealed by a decreased Zn/V elemental ratio from the transmission electron microscopy-dispersive spectrometry analysis (Fig. S23<sup>†</sup>). Moreover, the *in situ* X-ray diffraction measurement showed that the pronounced peak at  $\sim 25^\circ$  (Fig. 3d), attributed to the (1 0 0) plane of  $\text{V}_6\text{O}_{13}$ , gradually shifted to a larger angle at first and then remained almost unchanged.<sup>29,30</sup> This peak shift indicated a gradually decreased *d*-spacing, and further implied an exceptional deintercalation of  $\text{Zn}^{2+}$  ions from VCFs in the air-recharging process (Fig. 3e). This air-recharging reaction *via*  $\text{Zn}^{2+}$  deintercalation, and not *via* conversion as in previous active redox materials, may act as a reversal of the galvanostatic discharging process to afford sustained self-charging capability.

The one-dimensional porous structure of VCF was appreciated as a crucial merit conducive to the maximized exposure to the dissolved  $\text{O}_2$ . Indicated by rhodamine in the aqueous electrolyte, signals at different depths revealed that VCF was fully infiltrated with the electrolyte, as shown in the three-dimensional confocal laser scanning microscopy image (Fig. 4a). This sufficient contact between VCF and the aqueous electrolyte allowed accessible  $\text{O}_2$  dissolution for the oxidation of unsealed VCF. Galvanostatic discharge profiles were then measured for the electrochemical evaluation of air-recharged VCF (e.g.,  $\text{Zn}_{3.49-x}\text{V}_6\text{O}_{13}$ ). The air-recharging process afforded

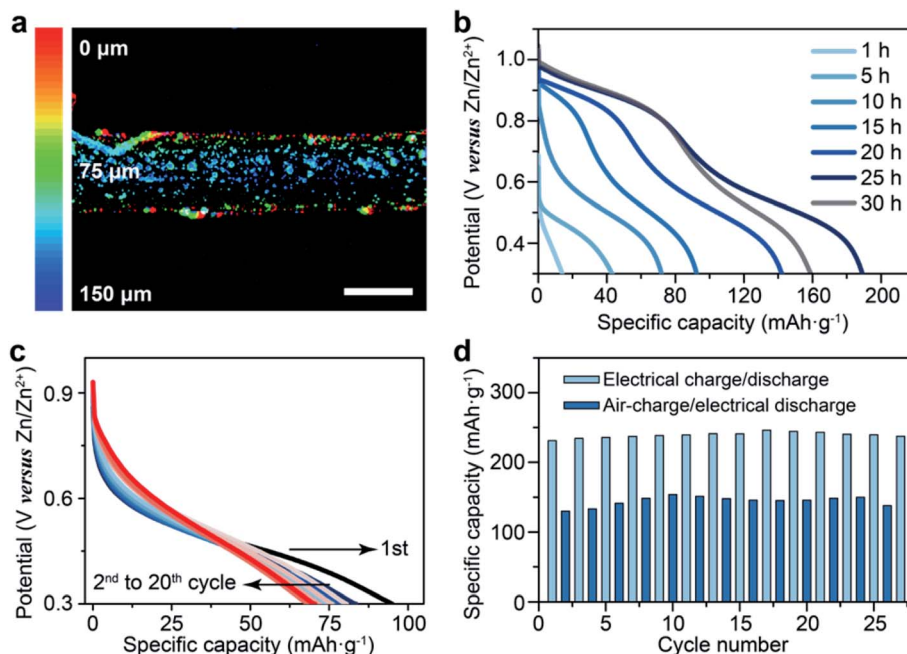


Fig. 4 (a) Three-dimensional confocal laser scanning microscopy image of VCF infiltrated with the aqueous electrolyte. The scanning depth was 150  $\mu\text{m}$  and 1% of rhodamine was added as the indicator. (b) Galvanostatic discharge curves of the Zn/Zn<sub>3.49-x</sub>V<sub>6</sub>O<sub>13</sub> battery fiber at 100 mA g<sup>-1</sup> upon its air-recharging process for numerous reaction times. (c) Repeated air-charging/galvanostatic discharging cycles of VCF/Zn battery fibers. (d) The cycling stability upon alternative charging/discharging operations of the VCF/Zn battery fiber. Scale bar, 200  $\mu\text{m}$  in (a).

an increasing discharge capacity of up to 191 mA h g<sup>-1</sup> upon the extension of the oxidation time for the first 25 h (Fig. 4b). The open-circuit voltage of VCFs accordingly increased (Fig. S24<sup>†</sup>) due to the deeper oxidation of Zn<sub>3.49-x</sub>V<sub>6</sub>O<sub>13</sub>. Further the extension of the air-recharging time (>25 h) would contribute little to the discharge capacity because the redox potential difference would gradually decrease until it is unable to drive the extraction of Zn<sup>2+</sup> (details in Note S3<sup>†</sup>).

The air-charging process was reversible, as revealed by the highly overlapped discharge curves recorded from the repeated air-charging/galvanostatic discharging cycles (Fig. 4c). When the air-recharging time was prolonged from 10 to 20 h and then reverted to 10 h, the discharge capacity could accordingly increase from 79 to 145 mA h g<sup>-1</sup> and then recovered to 76 mA h g<sup>-1</sup> (Fig. S25<sup>†</sup>). Furthermore, the air-recharging reaction of the VCF/Zn battery fiber was compatible with the routine galvanostatic charge–discharge. This was evidenced by the well-maintained discharging capacity upon the recurring alternative operation of air-recharging (20 h)/galvanostatic discharging (at 100 mA g<sup>-1</sup>) and galvanostatic charging/discharging (at 1 A g<sup>-1</sup>) processes (Fig. 4d and S26<sup>†</sup>). During the cycles, the ohmic resistance and the charge transfer resistance of VCFs remained almost unchanged upon repeated alternative operation processes (Fig. S27<sup>†</sup>). This implied the surface stability of VCFs upon the air-recharging process (Fig. S28<sup>†</sup>) as well as its compatibility with the routine charge–discharge. In addition, the air-recharged battery fiber could be further galvanostatically charged to its fully charged state (1.5 V) when the electrical power supply is available (Fig. S29<sup>†</sup>). Therefore, the air-recharging function could serve as a promising backup power

supply for the VCF/Zn battery fiber, enhancing its applicability towards wearable electronic applications.

From the device aspect, the air-recharging process of the VCF/Zn battery fiber was designed to be triggered by removing the impermeable encapsulation and diffusing air (O<sub>2</sub>). Specifically, a double-layer tubular encapsulation was customized for the air-rechargeable VCF/Zn battery fiber (Fig. 5a). The removable outer layer was composed of impermeable poly(vinyl ether) and O<sub>2</sub>-permeable low-density polyethylene (LDPE) was selected as the inner tubular encapsulation. In routine galvanostatic charge–discharge processes, the VCF/Zn battery fiber was protected by the double-layer tubular encapsulation without air permeability. Once the VCF/Zn battery fiber was exhausted, the air-recharging process could be initiated by the removal of the outer poly(vinyl ether) tube (in yellow). In this paradigm, the battery fiber was encapsulated by a single-layer of LDPE. Due to its nonpolar molecular structure, the flexible LDPE tube afforded a high selectivity for O<sub>2</sub> (~40 barrier for O<sub>2</sub> permeability) to enable the spontaneous oxidation reaction, meanwhile preventing electrolyte volatilization and moisture erosion (<0.9 g m<sup>-2</sup> d<sup>-1</sup> for H<sub>2</sub>O permeability).<sup>41</sup> Thus, the continuous O<sub>2</sub> diffusion could be permitted into the aqueous Zn(CF<sub>3</sub>SO<sub>3</sub>)<sub>2</sub> electrolyte and then react with the discharged VCF (e.g., Zn<sub>3.49</sub>V<sub>6</sub>O<sub>13</sub>) for capacity recovery.

To visualize the feasibility of this air-recharging capability, two aqueous VCF/Zn battery fibers were connected in series to power a thermometer. After their exhaustion (Fig. 5b), the battery fibers were unsealed in the ambient air for several hours and then they could be recharged to repower the thermometer (Fig. 5c). Impressively, leaving the air-recharged battery fiber in

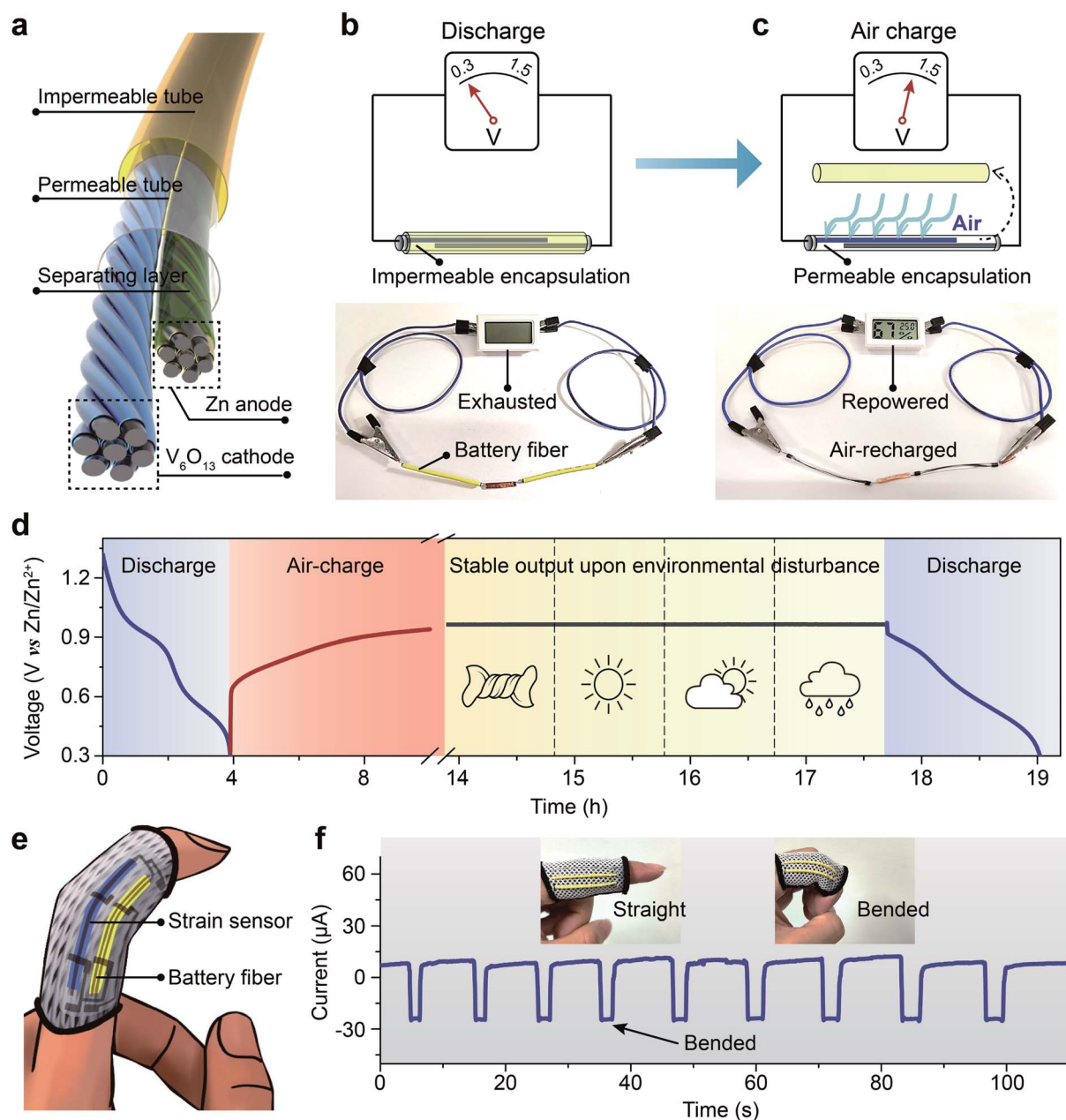


**Fig. 5** (a) A diagram of the flexible, double-layer-encapsulated VCF/Zn battery fiber. (b) and (c) A thermometer powered by two air-rechargeable VCF/Zn battery fibers connected in series at exhausted and air-recharged states, respectively. (d) The air-rechargeable VCF/Zn battery fiber showing a stable voltage output under numerous environmental disturbances. (e) A strain sensor fiber was powered by VCF/Zn battery fibers integrated in a flexible fingertip. (f) Current–time curve of the strain sensor fiber upon the increasing bending cycle.

varying practical scenarios, *e.g.*, upon deformations and all-weather conditions for hours did not show any significant voltage loss (Fig. 5d). The flexible fiber-shaped configuration also made it favorable for convenient integration with other functional modules that could fit into the irregular surface of human body. As a proof-of-concept, the VCF/Zn battery fibers were integrated with a strain sensor into a wearable fingertip (Fig. 5e). During the repeated curving of the finger, the strain sensor fiber could make immediate response (Fig. 5f), demonstrating the feasibility of this air-recharged battery fiber towards self-powering wearable systems.

## Conclusions

In summary, a high-performance aqueous Zn-ion battery fiber with air-recharging capability is achieved by synthesizing a  $V_6O_{13}/CNT$  cathode fiber through a facile solution-redox method. This rationally-designed VCF has overcome the canonical tradeoff between the self-charging activity and high specific capacity in self-rechargeable electrode materials. A configuration-based solution is further presented to enable stable and reversible operation of the flexible, air-rechargeable battery fiber by inhibiting the electrolyte volatilization and

ambient erosions. The resultant VCF/Zn battery fiber shows a high gravimetric capacity of  $371 \text{ mA h g}^{-1}$ , long cyclability up to 5000 cycles, and could be efficiently recharged to  $\sim 60\%$  with an open-circuit voltage of  $\sim 1.1 \text{ V}$  in ambient air. This study provides a new strategy to realize the self-powering functionality at material-level within simplified, flexible device configuration, contributing to the advancement of wearable electronic systems.

## Experimental section

### Synthesis of the $\text{V}_6\text{O}_{13}$ /CNT electrode fiber (VCF)

A two-step, solution-redox-based approach was adopted for the synthesis of freestanding VCFs. In step 1,  $\alpha\text{-MnO}_2$  nanoparticles were electrodeposited onto aligned CNT fibers in a three-electrode mode with a Pt counter electrode and an Ag/AgCl reference electrode. The electrodeposition was performed under a pulse electrodeposition mode (1.5 V for 1 s and 0.7 V for 10 s) in an aqueous solution containing  $0.1 \text{ mol L}^{-1} \text{ Mn}(\text{CH}_3\text{-COO})_2$  and  $0.1 \text{ mol L}^{-1} \text{ Na}_2\text{SO}_4$ . In step 2, the as-prepared  $\text{MnO}_2$ /CNT fiber was soaked in an aqueous  $\text{VO}_2^+$  solution ( $0.1 \text{ mol L}^{-1}$ ) overnight at room temperature. A layer of  $\text{V}_6\text{O}_{13}$  in faint blue could be observed on the surface of aligned CNT fibers after soaking. The obtained  $\text{V}_6\text{O}_{13}$ /CNT fiber was then thoroughly washed with deionized water to remove the remnant impurities (e.g.,  $\text{Mn}^{2+}$  and  $\text{MnO}_2$ ) and then allowed to be dried in air. The formation of nanostructured  $\text{V}_6\text{O}_{13}$  was driven by the difference of redox potentials between  $\text{MnO}_2/\text{Mn}^{2+}$  and  $\text{VO}_2^+/\text{VO}_2$ .<sup>26</sup> The normalized mass loading of  $\text{V}_6\text{O}_{13}$  in VCFs was measured to be  $\sim 1 \text{ mg cm}^{-2}$  by an electronic macro-balance (BT25S, 0.0001 mg).

### Fabrication and modification of the Zn anode

A facile electroplating method in a two-electrode mode was used to fabricate the Zn anode on aligned CNT fibers. The Zn electrodeposition was performed at  $-0.8 \text{ V}$  versus Zn foil (purity of  $>99.9\%$ , serving as both counter and reference electrodes) for  $\sim 1000 \text{ s}$  in an aqueous solution containing  $1 \text{ mol L}^{-1} \text{ ZnSO}_4$  and  $1 \text{ mol L}^{-1} \text{ KCl}$ . The Zn-coated CNT fibers were then washed with deionized water and then allowed to be dried at room temperature in vacuum for  $\sim 5 \text{ h}$  before use. A dispersion of 1 : 5 polyvinylidene fluoride/nano- $\text{CaCO}_3$  (weight) in an *N*-methyl pyrrolidone solvent was prepared and then uniformly coated onto the Zn-deposited CNT anode fibers to form a porous separating layer<sup>42</sup> after drying. The as-modified Zn anode fiber was accessible to the electrolyte and would not result in short circuits when assembled with VCF to produce the full battery fiber.

### Fabrication of the air-recharging VCF/Zn battery fiber

The fiber-shaped VCF/Zn battery was assembled using VCF as a cathode and the Zn-deposited CNT fiber as the anode. The two electrode fibers soaked with  $3 \text{ M Zn}(\text{CF}_3\text{SO}_3)_2$  aqueous electrolyte were first encased in an  $\text{O}_2$  permeable LDPE tube and sealed with ultraviolet curing adhesive at two ends. The as-fabricated battery fiber was further encapsulated by another removable

layer of a heat-shrinkable poly(vinyl ether) tube to eliminate the influence from ambient conditions on galvanostatic charge-discharge processes.

### Electrochemical measurements

Electrochemical tests were conducted on an Arbin multichannel electrochemical testing system (MSTAT-10 V, 10 mA, 32 channels).  $3 \text{ M Zn}(\text{CF}_3\text{SO}_3)_2$  aqueous electrolyte was used with a controlled dosage of  $\sim 40 \mu\text{L}$ . Cyclic voltammograms were recorded on a CHI 660E electrochemical station at  $0.1\text{--}1.0 \text{ mV s}^{-1}$  versus Zn/Zn<sup>2+</sup>. The electrochemical impedance measurement was conducted from 10 mHz to 1 MHz with a voltage amplitude of 5 mV. The applied current densities and specific capacity in the galvanostatic charge-discharge tests were calculated based on the mass of as-synthesized  $\text{V}_6\text{O}_{13}$  in VCF.

### Characterizations

The structure and morphology of VCF, aligned CNT fibers and the Zn-deposited anode fiber were characterized by scanning electron microscopy (Zeiss FE-SEM Ultra 55 operated at 3 kV) and transmission electron microscopy (JEOL JEM-2100F operated at 200 kV). Raman analysis was conducted on a Raman spectrometer (Dilor LabRam-1B, He-Ne laser of 4 mW, excitation wavelength of 532 nm). *Ex situ* XRD analysis was conducted on an X-ray power diffractometer (Bruker AXSD8) with filtered Cu  $K\alpha$  radiation. *In situ* XRD measurements were conducted using customized cells with a Be window on the surface for X-ray penetration. X-ray photoelectron spectra was recorded on a PHI5300 system (Mg, 250 W, 14 kV). A 3D laser confocal microscope image was recorded from Nikon C2<sup>+</sup>. Photographs were captured by a camera (SONY A6000, Japan).

## Author contributions

H. P. and B. W. conceived and designed the research project. M. L. performed the experiments on aqueous zinc-ion battery fibers. M. L., J. W., L. Y., H. S. and P. L. performed electrochemical measurements. C. T., C. W. and X. C. analyzed the data. And all the authors discussed the data and wrote the paper.

## Conflicts of interest

There are no conflicts to declare.

## Acknowledgements

This work was supported by MOST (2016YFA0203302), NSFC (21634003, 51573027, 51673043, 21604012), STCSM (16JC1400702, 17QA1400400, 18QA1400700), SHMEC (2017-01-07-00-07-E00062).

## References

- 1 H. Sun, Y. Zhang, J. Zhang, X. Sun and H. Peng, *Nat. Rev. Mater.*, 2017, **2**, 17023.

- 2 T. Khudiyev, J. T. Lee, J. R. Cox, E. Argentieri, G. Loke, R. Yuan, G. H. Noel, R. Tatara, Y. Yu, F. Logan, J. Joannopoulos, Y. Shao-Horn and Y. Fink, *Adv. Mater.*, 2020, **32**, 2004971.
- 3 L. Wang, X. Fu, J. He, X. Shi, T. Chen, P. Chen, B. Wang and H. Peng, *Adv. Mater.*, 2020, **32**, 1901971.
- 4 F. Mo, G. Liang, Z. Huang, H. Li, D. Wang and C. Zhi, *Adv. Mater.*, 2020, **32**, 1902151.
- 5 D. G. Mackanic, M. Kao and Z. Bao, *Adv. Energy Mater.*, 2020, **10**, 2001424.
- 6 L. Ma, Y. Zhao, X. Ji, J. Zeng, Q. Yang, Y. Guo, Z. Huang, X. Li, J. Yu and C. Zhi, *Adv. Energy Mater.*, 2019, **9**, 1900509.
- 7 M. Liao, L. Ye, Y. Zhang, T. Chen and H. Peng, *Adv. Electron. Mater.*, 2019, **5**, 1800456.
- 8 Z. Gao, P. Liu, X. Fu, L. Xu, Y. Zuo, B. Zhang, X. Sun and H. Peng, *J. Mater. Chem. A*, 2019, **7**, 14447–14454.
- 9 N. Zhang, F. Huang, S. Zhao, X. Lv, Y. Zhou, S. Xiang, S. Xu, Y. Li, G. Chen, C. Tao, Y. Nie, J. Chen and X. Fan, *Matter*, 2020, **2**, 1260–1269.
- 10 J. Chen, Y. Huang, N. Zhang, H. Zou, R. Liu, C. Tao, X. Fan and Z. L. Wang, *Nat. Energy*, 2016, **1**, 16138.
- 11 K. Dong, Y. Wang, J. Deng, Y. Dai, S. L. Zhang, H. Zou, B. Gu, B. Sun and Z. L. Wang, *ACS Nano*, 2017, **11**, 9490–9499.
- 12 J. Lv, I. Jeerapan, F. Tehrani, L. Yin, C. A. Silva-Lopez, J. Jang, D. Joshuaia, R. Shah, Y. Liang, L. Xie, F. Soto, C. Chen, E. Karshalev, C. Kong, Z. Yang and J. Wang, *Energy Environ. Sci.*, 2018, **11**, 3431–3442.
- 13 J. Wang, L. Zhang, L. Yu, Z. Jiao, H. Xie, X. W. Lou and X. Sun, *Nat. Commun.*, 2014, **5**, 4921.
- 14 H. Zhang, Y. Yu, L. Zhang, Y. Zhai and S. Dong, *Chem. Sci.*, 2016, **7**, 6721–6727.
- 15 J. Zhao, Y. Tian, Z. Wang, S. Cong, D. Zhou, Q. Zhang, M. Yang, W. Zhang, F. Geng and Z. Zhao, *Angew. Chem., Int. Ed.*, 2016, **55**, 7161–7165.
- 16 Z. Bi, X. Li, Y. Chen, X. Xu, S. Zhang and Q. Zhu, *Electrochim. Acta*, 2017, **227**, 61–68.
- 17 B. Yang, D. Ma, E. Zheng and J. Wang, *Sol. Energy Mater. Sol. Cells*, 2019, **192**, 1–7.
- 18 Y. Zhang, F. Wan, S. Huang, S. Wang, Z. Niu and J. Chen, *Nat. Commun.*, 2020, **11**, 2199.
- 19 D. Kundu, B. D. Adams, V. Duffort, S. H. Vajargah and L. F. Nazar, *Nat. Energy*, 2016, **1**, 16119.
- 20 F. Wan, S. Huang, H. Cao and Z. Niu, *ACS Nano*, 2020, **14**, 6752–6760.
- 21 S. Guo, L. Qin, T. Zhang, M. Zhou, J. Zhou, G. Fang and S. Liang, *Energy Storage Mater.*, 2021, **34**, 545–562.
- 22 B. Tang, L. Shan, S. Liang and J. Zhou, *Energy Environ. Sci.*, 2019, **12**, 3288–3304.
- 23 H. Liang, Z. Cao, F. Ming, W. Zhang, D. H. Anjum, Y. Cui, L. Cavallo and H. N. Alshareef, *Nano Lett.*, 2019, **19**, 3199–3206.
- 24 C. Wang, T. He, J. Cheng, Q. Guan and B. Wang, *Adv. Funct. Mater.*, 2020, **30**, 2004430.
- 25 L. Ye, M. Liao, T. Zhao, H. Sun, Y. Zhao, X. Sun, B. Wang and H. Peng, *Angew. Chem., Int. Ed.*, 2019, **58**, 17054–17060.
- 26 Y.-L. Ding, Y. Wen, C. Wu, P. A. van Aken, J. Maier and Y. Yu, *Nano Lett.*, 2015, **15**, 1388–1394.
- 27 J. Ding, Z. Du, B. Li, L. Wang, S. Wang, Y. Gong and S. Yang, *Adv. Mater.*, 2019, **31**, 1904369.
- 28 D. Chao, W. Zhou, C. Ye, Q. Zhang, Y. Chen, L. Gu, K. Davey and S. Qiao, *Angew. Chem., Int. Ed.*, 2019, **58**, 7823–7828.
- 29 P. Liu, K. Zhu, Y. Gao, H. Luo and L. Lu, *Adv. Energy Mater.*, 2017, **7**, 1700547.
- 30 P. He, J. Liu, X. Zhao, Z. Ding, P. Gao and L. Fan, *J. Mater. Chem. A*, 2020, **8**, 10370–10376.
- 31 Y. Zhang, Y. Wang, L. Wang, C.-M. Lo, Y. Zhao, Y. Jiao, G. Zheng and H. Peng, *J. Mater. Chem. A*, 2016, **4**, 9002–9008.
- 32 Z. Guo, Y. Zhao, Y. Ding, X. Dong, L. Chen, J. Cao, C. Wang, Y. Xia, H. Peng and Y. Wang, *Chem*, 2017, **3**, 348–362.
- 33 Y. Wang, D. Kong, S. Huang, Y. Shi, M. Ding, Y. Von Lim, T. Xu, F. Chen, X. Li and H. Y. Yang, *J. Mater. Chem. A*, 2018, **6**, 10813–10824.
- 34 H. Li, Z. Liu, G. Liang, Y. Huang, Y. Huang, M. Zhu, Z. Pei, Q. Xue, Z. Tang, Y. Wang, B. Li and C. Zhi, *ACS Nano*, 2018, **12**, 3140–3148.
- 35 F. Wan, L. Zhang, X. Wang, S. Bi, Z. Niu and J. Chen, *Adv. Funct. Mater.*, 2018, **28**, 1804975.
- 36 Q. Zhang, C. Li, Q. Li, Z. Pan, J. Sun, Z. Zhou, B. He, P. Man, L. Xie, L. Kang, X. Wang, J. Yang, T. Zhang, P. P. Shum, Q. Li, Y. Yao and L. Wei, *Nano Lett.*, 2019, **19**, 4035–4042.
- 37 S. Deng, Z. Yuan, Z. Tie, C. Wang, L. Song and Z. Niu, *Angew. Chem., Int. Ed.*, 2020, **59**, 22002–22006.
- 38 C. Xia, J. Guo, P. Li, X. Zhang and H. N. Alshareef, *Angew. Chem., Int. Ed.*, 2018, **57**, 3943–3948.
- 39 M. Liao, J. Wang, L. Ye, H. Sun, Y. Wen, C. Wang, X. Sun, B. Wang and H. Peng, *Angew. Chem., Int. Ed.*, 2020, **59**, 2273–2278.
- 40 H. Li, L. McRae, C. J. Firby and A. Y. Elezzabi, *Adv. Mater.*, 2019, **31**, 1807065.
- 41 L. Wang, J. Pan, Y. Zhang, X. Cheng, L. Liu and H. Peng, *Adv. Mater.*, 2018, **30**, 1704378.
- 42 L. Kang, M. Cui, F. Jiang, Y. Gao, H. Luo, J. Liu, W. Liang and C. Zhi, *Adv. Energy Mater.*, 2018, **8**, 1801090.